Spin reorientation induced anisotropic magnetoresistance switching in LaCo$_{0.5}$Ni$_{0.5}$O$_{3-\delta}$ thin films

P. K. Sreejith [1,2,*], T. S. Suraj [3], Hari Babu Vasili,[4] Suresh Sreya,[2] Pierluigi Gargiani,[5] K. Sethupathi [1,6]
Oscar Cespedes,[4] V. Sankaranarayanan,[1] and M. S. Ramachandra Rao [2,6,†]

[1]*Department of Physics, Low Temperature Physics Laboratory, Indian Institute of Technology Madras, Chennai 600036, India*
[2]*Department of Physics, Nano Functional Materials Technology Center, Material Science Research Center,*
Indian Institute of Technology Madras, Chennai 600036, India
[3]*Department of Physics, National University of Singapore, 2 Science Drive 3, 117551 Singapore*
[4]*School of Physics and Astronomy, W. H. Bragg Building, University of Leeds, Leeds LS2 9JT, United Kingdom*
[5]*ALBA Synchrotron Light Source, E-08290 Cerdanyola del Vallès, Barcelona, Catalonia, Spain*
[6]*Quantum Centre of Excellence for Diamond and Emergent Materials (QuCenDiEM),*
Indian Institute of Technology Madras, Chennai 600036, India

Realization of diverse functionalities by tuning magnetic interactions in rare-earth perovskite oxide thin films opens up exciting technological prospects. Strain-induced tuning of magnetic interactions in rare-earth cobaltates and nickelates is of central importance due to their versatility in electronic transport properties. Here we report the spin reorientation induced switching of anisotropic magnetoresistance (AMR) and its tunability with strain in epitaxial LaCo$_{0.5}$Ni$_{0.5}$O$_{3-\delta}$ thin films across the ferromagnetic transition. Moreover, with strain tuning, we observe a twofold to fourfold symmetry crossover in AMR across the magnetic transition temperature. The magnetization measurements reveal a ferromagnetic transition around 50 K. At temperatures below this transition, there is a subtle change in the magnetization dynamics, which reduces the ferromagnetic long-range ordering in the system. X-ray absorption and x-ray magnetic circular dichroism spectroscopy measurements at the Co and Ni L edges reveal a Co spin state transition below 50 K, leading to the AMR switching and also the presence of Ni^{2+} and Co^{4+} ions evidencing the charge transfer from Ni to Co ions. Our work demonstrates the tunability of magnetic interactions mediated electronic transport in cobaltate-nickelate thin films, which is relevant in understanding Ni-Co interactions in oxides for their technological applications such as in AMR sensors.

I. INTRODUCTION

Transition metal oxides have generated great interest for their exciting magnetic and electrical properties such as superconductivity, colossal magnetoresistance, metal-insulator (M-I) transitions, and large anisotropic magnetoresistance (AMR) [1]. AMR observed in ferromagnetic (FM) materials is usually associated with a change in the electron-scattering rate depending upon the orientation of the magnetization with the applied current [2–8]. AMR property has been utilized in spintronic applications and, more recently, in probing Fermi surface topology [9,10].

Transition metal oxides LaNiO$_3$ (LNO) and LaCoO$_3$ (LCO) are of particular interest for their charge, orbital, and spin state correlations [11,12]. LNO is a highly correlated paramagnetic metal oxide, whereas LCO is a diamagnetic Mott insulator having temperature-dependent multiple spin-state transitions [11,13,14]. In LCO, the nonmagnetic insulating ground state is due to the fully occupied low-spin (LS) state of the trivalent cobalt ion. As the temperature

increases, the fully localized electrons in the t_{2g} level undergo spin-state transitions from a low-spin to an intermediate-spin (IS) state at about 90 K, and then to high-spin (HS) state beyond 500 K [15–20]. The temperature dependence of the Co^{3+} spin states can be attributed to the comparable crystal field splitting energy (10 Dq) and the Hund's exchange energy. These various ground states in LCO can be tuned by doping with other transition elements such as Ni, Mn, and Fe [21,22].

Solid solutions of rare-earth cobaltate and nickelate perovskites are found to exhibit spin-glass behavior [23,24]. Spin-glass behavior arises due to competing FM and antiferromagnetic interactions. Ferromagnetism arises from the double exchange interaction of Co^{3+}-O-Co^{4+} whereas antiferromagnetism arises from the superexchange interactions arising from Co^{3+}-O-Co^{3+} and Ni^{3+}-O-Ni^{3+} [25]. Usually, large negative magnetoresistance is associated with spin-glass systems because of the growth of FM domains in the presence of an external magnetic field that in turn promotes metallic conduction through the double exchange hopping mechanism [24,26]. In thin films, the influence of strain parameters further enhances the electrical transport and magnetic properties. Confinement effects have a profound impact on electronic transport, magnetoresistance (MR), and AMR [27]. The emergence of long-range ferromagnetism in thin-film manganites

_____
*sreejithpksr@gmail.com
†msrrao@iitm.ac.in

is one example [28]. Tuning the electrical and magnetic properties of LCO by Ni doping in the Co site has been well studied in polycrystalline bulk form [21,23]. However, studies on single crystals and epitaxial thin films are required to understand the role of magnetocrystalline anisotropy and strain effects in the electronic transport mechanism of a Ni-doped LCO system.

In this work, we discuss the microscopic origin of large positive magnetoconductance and anisotropic magnetoresistance switching in $LaCo_{0.5}Ni_{0.5}O_{3-\delta}$ (LCNO) thin films. Electrical transport measurements combined with x-ray absorption spectroscopy and magnetometry were used to elucidate the interplay of complex magnetic order and electron correlations. The paper is organized as the following sections: Section II deals with the experimental techniques used in this work. Section III consists of four parts. In Sec. III A, we discuss the structural and strain parameters of LCNO thin films. Section III B deals with electrical transport properties, where we discuss the enhanced negative MR in epitaxially strained thin films. In Sec. III C, we discuss angle-dependent magnetoresistance measurements. In Sec. III D, we discuss the magnetic properties, followed by the discussions on the electronic spin-state transitions associated with the multivalent states of Co and Ni ions through x-ray absorption spectroscopy (XAS) and x-ray magnetic circular dichroism (XMCD) measurements in Sec. III E.

II. EXPERIMENTAL METHODS

Bulk polycrystalline LCNO target material for thin-film deposition was synthesized using the conventional citrate-based sol-gel technique [29]. The final product thus obtained was cold-pressed into a pellet and sintered at 900 °C for 24 h. Thin films of LCNO with various thicknesses were grown on TiO_2-terminated $SrTiO_3$ (001) (STO) substrates with the help of the pulsed laser deposition technique. A 248-nm KrF laser source was used with laser fluence of 2 J cm^{-2} and a pulse repetition rate of 3 Hz. The base pressure of the deposition chamber was set at 3×10^{-5} mbar and during deposition, a constant flow of high-purity oxygen (99.999%) O_2 with a partial pressure of 2×10^{-1} mbar was maintained. The substrate temperature was kept at 700 °C. Post deposition, while cooling down to RT, 100-mbar O_2 partial pressure was maintained inside the deposition chamber to ensure proper oxygen stoichiometry.

The phase purity of thin-film samples was confirmed using a high-resolution x-ray diffractometer (Rigaku Smart Lab II) with a Cu $K\alpha$ source ($\lambda = 1.54$ Å). 2θ-ω scans were done around the (200) peak of the STO substrate. From x-ray reflectivity (XRR) measurements, film thickness and roughness were determined. In order to study in-plane strain due to sample-substrate lattice mismatch, reciprocal space mapping (RSM) was carried out along the pseudocubic $(103)_{pc}$ crystal plane of the STO. Electrical transport measurements were carried out using a commercial physical property measurement system (PPMS; Quantum Design) from 300 K down to 2 K using the standard linear four-probe method. The contacts were aligned along the [010] direction of the crystal. Field-dependent measurements were carried out with varying magnetic fields up to 9 T. Angle-dependent MR was

carried out using the commercially available rotating holder attachment. Magnetization measurements were carried out in a superconducting quantum interference device (SQUID) based vibrating sample magnetometer (MPMS XL, Quantum Design). X-ray absorption spectroscopic measurements were carried out to investigate the magnetization and valence states of the transition elements. XAS and XMCD measurements were carried out at the BL-29 BOREAS beamline of the ALBA synchrotron light source [30]. The XMCD spectra were obtained by taking the difference between the XAS of right (σ^+) and left (σ^-) circularly polarized light. The samples were measured in the in-plane geometry (grazing incidence from the film plane) under an applying magnetic field of 6 T in the beam direction. The data were collected in the total electron yield mode.

III. RESULTS AND DISCUSSION

A. Structural and morphological characterization

Bulk LCNO has a rhombohedral ($R\bar{3}c$) structure [23]. Figure 1(a) shows the room-temperature x-ray diffraction 2θ-ω scan of the LCNO film grown on STO(001) substrate. The observation of Kiessig fringes in the 2θ-ω x-ray diffractogram confirms the good crystallinity of the films. To determine the film thickness, x-ray reflectometry (XRR) measurements were done and fitted with GenX software as shown in Fig. 1(c) [31]. The fit gives an average surface roughness (r_a) of ~5 Å for as-grown films. The bulk pseudocubic (pc) lattice parameter for LCNO is found to be 3.789 Å. On STO substrate, the out-of-plane lattice parameter of the LCNO thin film is found to be 3.801 Å. Further, from the RSM plots of $(103)_{pc}$ Bragg planes [see Fig. 1(b)], the in-plane and out-of-plane strain parameters relative to that of STO ($a_{pc} = 3.90$ Å) were found to be 0.25% and 2.8% tensile strained, respectively, for 25-nm-thick film. A rocking curve scan for the film shows a FWHM of 0.19°, again indicating good crystallinity of the film [shown in Fig. 1(d)]. The perovskite film is epitaxially oriented, grown along the [00l] direction of the STO substrate as shown in Fig. 1.

B. Electrical transport properties

Temperature- and magnetic field–dependent electrical transport properties of LCNO films have been investigated down to 2 K. Temperature dependence of resistivity shows three-dimensional (3D) Mott variable range hopping below 150 K. A detailed analysis is given in the Appendix A.

Magnetic field-dependent resistivity measurements reveal large negative magnetoresistance in LCNO films. Though there can be multiple origins for negative magnetoresistance, in general, it can be attributed to the weak localization caused by the interference of the electron wave functions facilitated by the time-reversal symmetry breaking due to the onset of ferromagnetic ordering below the transition temperature. Applying an external magnetic field will create a phase shift between the electron wave functions and lift the localization. This results in a decrease in the resistivity of the system [32]. Magnetoconductance (ΔG) measurements were taken for LCNO thin films of thickness 10 and 25 nm, with field varying from -9 to 9 T. The magnetoconductance data
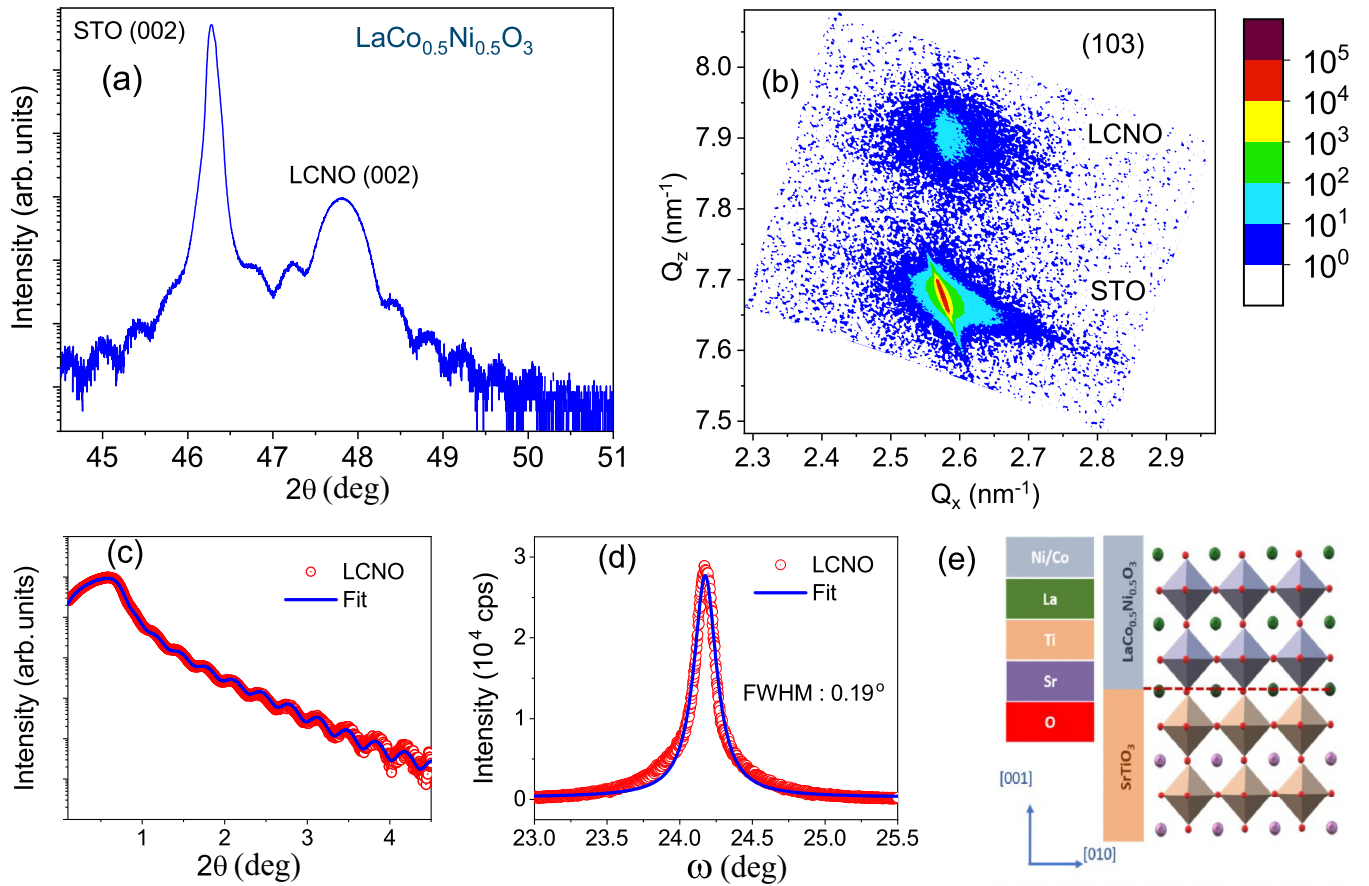
FIG. 1. Structural characterization. (a) Thin-film XRD data of LCNO film on SrTiO$_3$ substrate with (002) peaks indexed. (b) RSM of the LCNO film along the (103) pseudocubic plane. (c) Experimental XRR data (red open circles) for LCNO with a blue line indicating the fit. From the fit, the film thickness and surface roughness were found to be 25 and 0.5 nm, respectively. (d) XRD ω rocking curve of LCNO (002) peak (red open circles) with a Lorentzian fit (blue line). The FWHM is found to be 0.19°. (e) Schematic of LCNO stacking along the [001] direction.

were fitted with a simplified Hikami-Larkin-Nagaoka (HLN) equation within the spin-orbit coupling limit [33]. In the high-field region, magnetoconductance is dominated by the elastic electron-electron scattering, and hence a quadratic B^2 field dependence is incorporated into the HLN equation, which thus can be written as

$$\Delta G(B) = \frac{e^2}{2\pi^2\hbar}\left[\psi\left(\frac{1}{2} + \frac{B_\varphi}{B}\right) - \ln\left(\frac{B_\varphi}{B}\right)\right] + AB^2, \quad (1)$$

where ψ is digamma function, B_φ is the effective field of inelastic scattering terms and is equal to $(\frac{\hbar}{4el_\varphi})^2$, l_φ is the phase coherence length, and A is the electron-electron interaction coefficient.

In Fig. 2(a), the experimentally obtained conductivity of a 10-nm thin film has been fitted with Eq. (1). A magnetoconductance maximum is obtained at the ordering temperature [see Fig. 2(b)]. Figure 2(c) gives the temperature dependence of inelastic phase coherence length, l_φ, and the electron-electron interaction coefficient A. It is interesting to note that there is no monotonous increase or decrease in l_φ and A. Instead, both parameters maximize near the ordering temperature and fall on either side. Correlation between the magnetoconductance maxima and l_φ can be understood based

on the ferromagnetic ordering of spins. The ferromagnetic alignment will reduce electron-electron scattering, which in turn increases l_φ. At low temperatures, some of the spins will reorient themselves antiparallel and the long-range ordering is reduced, with the possible emergence of a glassy phase. It is known that in spin-glass systems, the randomly fixed spins can dephase weak localization of electrons due to a reduction in magnetic scattering rate followed by suppression of the magnetic moment [34–36]. Thus we see a reduction in l_φ [see Fig. 2(b)]. A is added to the HLN equation to account for electron-electron elastic scattering and the classical cyclotron term. Based on the variations in the electron-scattering cross section due to ferromagnetic alignment followed by spin reorientation, the term A follows a similar trend as l_φ because of its direct correspondence to the electron-scattering cross-section variation. Linear magnetoresistance data were taken for magnetic field sweeps from −9 to +9 T. By taking the difference of the MR data in the two magnetic field sweep directions opposite to each other, we were able to deduce the magnetic field-dependent Hall resistance. By this procedure, in effect, we are removing the large linear magnetoresistance background. Figure 2(d) shows the Hall carrier concentration, n_H, which is extracted by fitting the slope of the linear region of Hall resistance, and Fig. 2(e) Hall carrier mobility, μ_H,
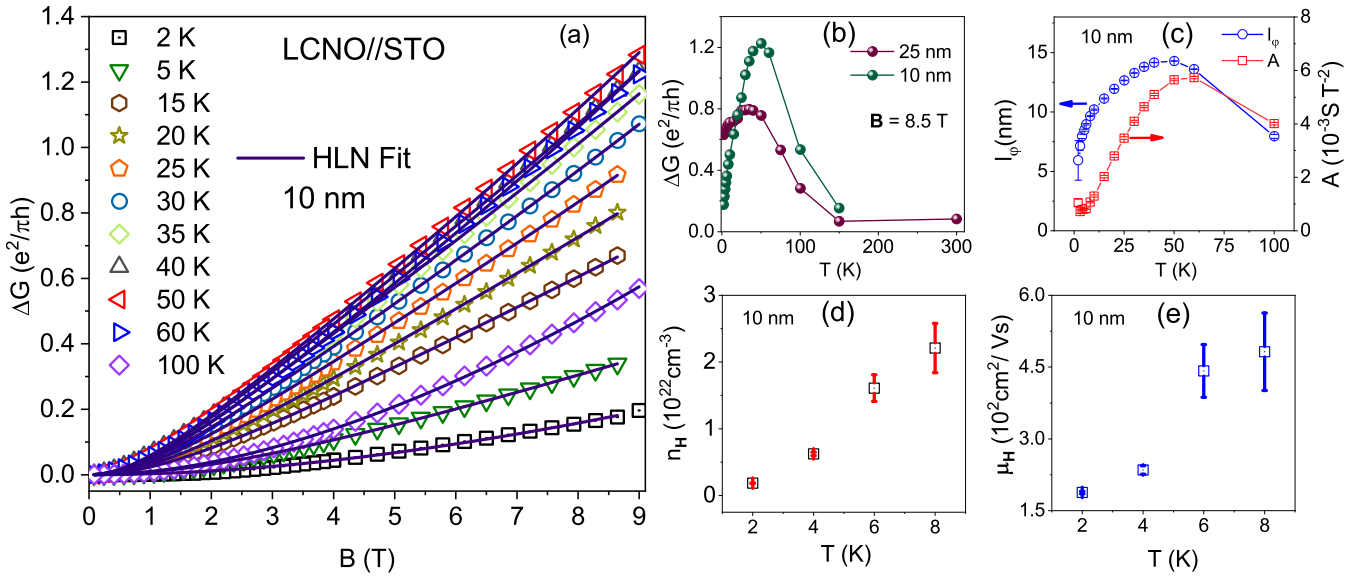
FIG. 2. Magnetoconductance [(a)–(c)] and Hall effect measurements [(d),(e)]. (a) Experimental magnetoconductance (ΔG) data (open symbols) and its corresponding fit (solid lines) to the Hikami-Larkin-Nagaoka equation with an additional electron-electron interaction term. (b) Temperature dependence of magnetoconductance for 25 and 10 nm films, respectively. (c) Inelastic scattering length (l_φ) and quadratic coefficient A, considering the B^2 dependence at high magnetic fields, both as a function of temperature. (d) Hall carrier concentration and (e) Hall carrier mobility as a function of temperature.

respectively, with respect to temperature. The Hall carrier concentration is high, of the order of 10^{22} cm^{-3}, which is similar to that of metals. However, the Hall mobility is very low, of the order of 10^2 cm^2 V^{-1} s^{-1}, which can be associated to the localization of electrons.

C. Anisotropic magnetoresistance switching

1. Origins of AMR in LCNO

AMR contains two components, crystalline and noncrystalline, where the former depends on the anisotropy of the electronic structure and spin-orbit coupling while the latter depends on the angle between the magnetization and current [37]. The origins of the AMR can be directly correlated to the Fermi surface [5]. Applying a magnetic field will change the free-electron trajectories near the anisotropic Fermi surface [38]. For a uniformly magnetized system, the total free energy per unit volume as a function of the angle ϕ between the magnetization and current direction can be given as [6]

$$E(\phi) = K_{\text{shape}} \sin^2 \phi - \mu_0 \boldsymbol{M}_s \cdot \boldsymbol{H} \cos(\phi - \theta)$$
$$+ K_{\text{cry}} \cos^2(\phi - \alpha), \quad (2)$$

where $\boldsymbol{H}$ is the applied magnetic field, $\boldsymbol{M}_s$ is the saturation magnetization, K_{shape} is the shape anisotropy constant related to the demagnetization factor, K_{cry} is the magnetocrystalline anisotropic constant, α is the angle defining the crystallographic directions, and θ is the angle between the applied magnetic field and current direction, which at high enough magnetic fields can be approximated to ϕ. Minimizing the free energy and approximating $\phi = \theta$, one can obtain the anisotropic magnetoresistance as

$$\rho_{\text{AMR}} = \rho_\perp + (\rho_\parallel - \rho_\perp) \cos^2 \theta, \quad (3)$$

where $\rho_\perp$ and $\rho_\parallel$ are the resistivity at $\boldsymbol{M}$ perpendicular and parallel to the applied current, respectively. The AMR is

therefore strongly dependent on $\cos^2 \theta$. This is generally valid for polycrystalline ferromagnetic materials. In the case of single-crystalline and low-dimensional epitaxial films with crystalline symmetry, magnetocrystalline effects need to be addressed [39]. LCNO films grown along the [001] orientation have a cubic fourfold symmetry and an additional fourfold term representing the crystalline symmetry contributes towards AMR, thus modifying Eq. (3) [40]:

$$\rho_{\text{AMR}} = A_0 + A_2 \cos[2(\theta + \theta_0)] + A_4 \cos[4(\theta + \theta_0)], \quad (4)$$

where A_2 and A_4 are the respective amplitudes of twofold and fourfold symmetry and θ_0 accounts for the misalignment due to the sample rotator. Angle-dependent magnetoresistance (ADMR) measurements were done on LCNO thin films in both γ (B rotating along the yz plane where current I is along the y axis) and β configurations (B rotation along the xz plane with current I in the y direction). Figure 3(a) shows the AMR, with an applied magnetic field of 9 T, at various temperatures taken by rotating the applied magnetic field direction with respect to the c axis of the crystal. The AMR percentage is calculated as

$$\frac{\rho(\theta) - \rho(\perp)}{\rho(\perp)} \times 100\%. \quad (5)$$

Here the magnetic field is applied along the [001] crystallographic direction. Both γ and β configurations show a similar trend in the AMR.

Temperature-dependent ADMR studies have shown a large AMR in LCNO thin films (see Fig. 3). In the LaCo$_{1-x}$Ni$_x$O$_3$ system, the M-I transition occurs at $x = 0.4$ and hence LCNO, with $x = 0.5$, is close to this M-I transition and a large AMR is expected [6,21]. In analogy to doped manganites, a disordered system like LCNO can be considered to have a conducting phase due to LNO and an insulating phase due to LCO. In
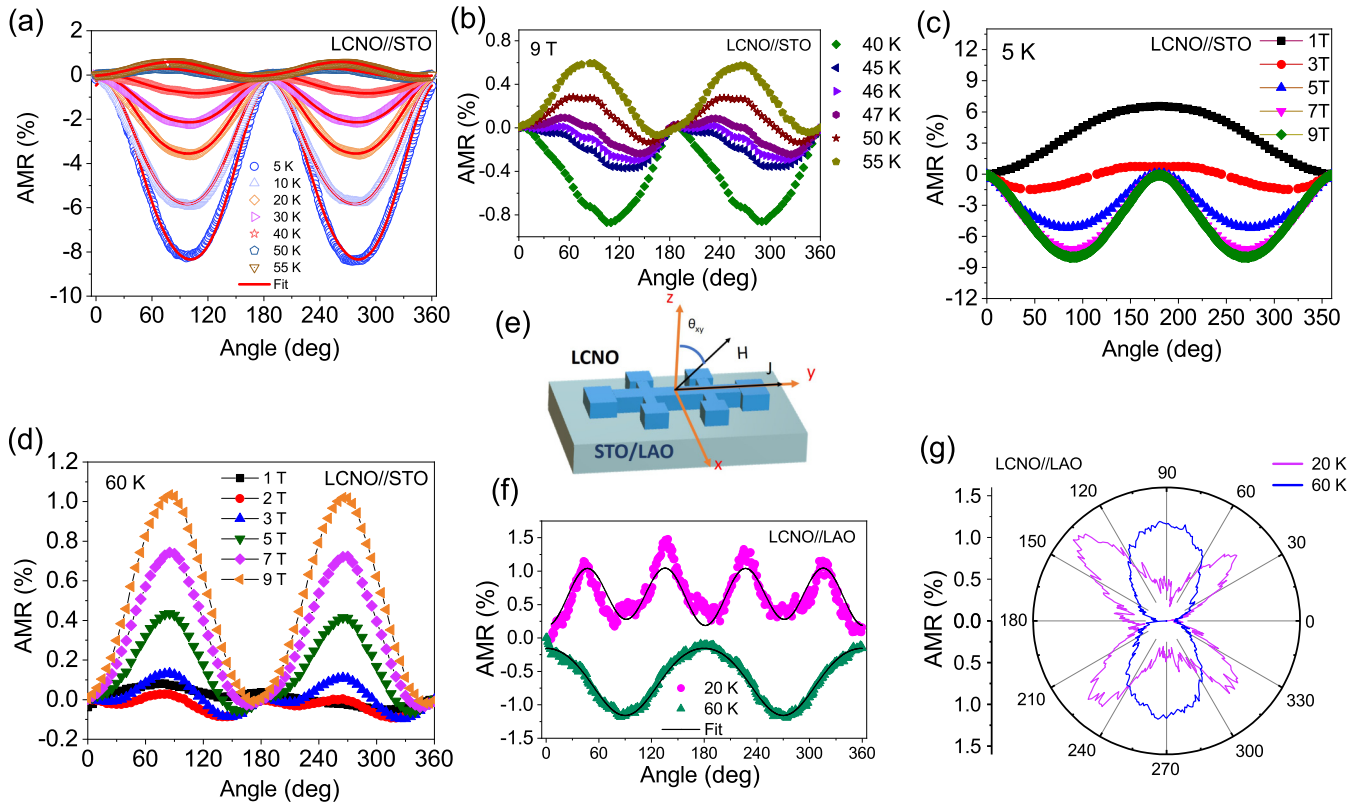
FIG. 3. AMR plots of LCNO films of 25 nm thickness grown on STO (a)–(d) and LAO (f),(g) substrates. (a) Temperature dependence of anisotropic magnetoresistance (AMR) of LCNO thin films for an applied field of 9 T, on STO substrate (open symbols), fitted with Eq. (4) (solid lines). (b) AMR data close to the transition temperature. (c) Field dependence of AMR below the magnetic transition temperature. (d) Field dependence of AMR above the magnetic transition temperature. (e) Schematic drawing of the magnetic field rotation with respect to crystal plane and applied current (γ configuration). (f) Temperature dependence of AMR in LAO substrate (with 9 T applied field). (g) Polar plots showing the twofold to fourfold symmetry crossover in LCNO films grown on LAO.

thin films, due to film-substrate lattice mismatch, there will be an enhancement in the phase separation between these metallic and insulating phases. This, in turn, will enhance the anisotropic character of magnetoresistance in the system. In the LCNO system, there is also a temperature-dependent sign reversal of the AMR around 45 K from positive (above 50 K) to negative (below 40 K) [see Figs. 3(a) and 3(b)]. In Figs. 3(c) and 3(d) field-dependent variations of the AMR are shown at 5 and 60 K (below and above the magnetic ordering temperature), respectively. The field-dependent evolution of AMR shows that only above 3 T magnetic field, do the twofold and fourfold components of the AMR set in. At low fields, the demagnetization effects will destroy the effective AMR. Unlike some manganite systems, we could not observe field-dependent AMR switching [6,41].

2. Spin-polarized scattering and the sign of AMR

The temperature-dependent sign reversal in AMR can be understood based on the change in the density of states of spin-up and spin-down conduction electrons above and below the magnetic transition. In ferromagnetic materials, due to spin polarization, the electron-scattering cross section will be spin dependent. According to the microscopic theory, AMR can be defined as $\rho_{AMR} = \gamma(\beta - 1)$, where γ is the spin-orbit coupling constant, which for most transition metals is

about 0.01 and β is the ratio of the spin-down to spin-up electron resistivity. Thus the sign of β determines whether AMR is negative or positive [42–44]. Hence in the case of LCNO, switching of positive to negative AMR values as the temperature is lowered across the transition temperature can be understood as a shift in the density of states of spin-up and spin-down conduction electrons, which will affect their respective resistivities. A similar sign reversal in AMR is also observed in doped manganite systems [6,41].

3. Low-temperature spin reorientation and AMR sign reversal

Below 50 K, there is a decrease in the net magnetization attributed to a possible spin reorientation and the emergence of glassy phase well below 45 K as seen in bulk LCNO [23]. Above 45 K, ferromagnetism causes spin polarization and the majority of electrons will be spin-up causing a reduction in the spin-up electron scattering leading to a positive AMR, which is in agreement with the magnetoconductance and magnetic data. Below 45 K, the long-range ferromagnetic ordering is lost due to spin reorientation changing the spin polarization, and the AMR becomes negative. It should be noted that at low enough temperatures, some of the Co^{3+} ions in LCNO have a spin-state transition from HS/IS state to LS state as evidenced from the XMCD measurements on the Co L_3 edge. This will reduce the overall ferromagnetism in the system because in

the LS state, the e_g orbitals are vacant. These vacant e_g orbitals will contribute towards the antiferromagnetic superexchange interaction and, in turn, will lead to the formation of a glassy phase in the system.

4. Strain dependence of AMR

The magnetocrystalline anisotropy and AMR are highly sensitive to strain. In order to understand the effects of strain on LCNO, we have also grown LCNO films ($\sim$25 nm thick) on [001]-oriented LaAlO$_3$ (LAO) substrates. Compared to films grown on tensile STO substrates, films grown on LAO are compressively strained, which is evident from the XRD plot given in Appendix B (see Fig. 9). From Fig. 3(f) we can see a clear distinction of LAO grown LCNO films, from its STO counterpart, in form of a crossover from twofold to fourfold symmetry at 60 and 20 K, respectively. Figure 3(g) shows the polar plot for the AMR shown in Fig. 3(f), where the twofold to fourfold distinction is very evident. AMR studies on (GaMn)As epitaxial films have shown that the origin of fourfold symmetry is related to the long-range ferromagnetic ordering below the transition temperature, T_C [39]. Further, in LCNO films grown on LAO, low-temperature AMR at 20 K is positive while AMR at 60 K is negative. So we can infer that the spin dynamics are different for compressively grown LCNO films.

D. Magnetic properties

Doping with trivalent transition metal ions in LCO is known to change the spin state of Co^{3+} in the system. However, Ni^{3+} in LNO remains at a low spin state throughout the temperature range, which is also the case for LCNO as evidenced from the XAS measurements given in the next section [45,46]. The presence of Ni ions in LCNO induces a change in Co^{3+} spin state from low spin to intermediate spin or high-spin state. The charge transfer between Ni and Co ions induces ferromagnetism in the system. Magnetization measurements, both temperature and field dependent, were done on LCNO films. Figure 4 shows the temperature-dependent magnetization when zero-field cooled (ZFC) and field cooled (FC), for a 25-nm-thick LCNO film on STO substrate for an out-of-plane 1000 Oe applied field. The data presented here are corrected for the diamagnetic contribution from the substrate by subtracting a constant diamagnetic moment obtained by fitting the high-field magnetization $M(H)$ data of STO substrate. But this approach may not completely remove the substrate contribution, especially at low temperatures where the magnetic moment is not completely temperature independent. In line with reports of the properties of the bulk material, there is a ferromagnetic transition at around 50 K as evidenced by the temperature-dependent magnetization measurements. However, as the temperature is lowered, the magnetization does not follow a Brillouin-like curve. Instead, the overall moment is reduced at low temperatures below 50 K, which could be due to possible spin reorientation [23]. From the bifurcation of ZFC-FC curves, which indicates magnetic anisotropy, it is clear that the formation of the ferromagnetic cluster in the system starts way before the magnetic transition temperature in the system. This unusual magnetic order arises from Co to Ni charge transfer resulting in the formation of Co^{4+} states and the Co^{3+}-O-Co^{4+} double exchange interaction leading to
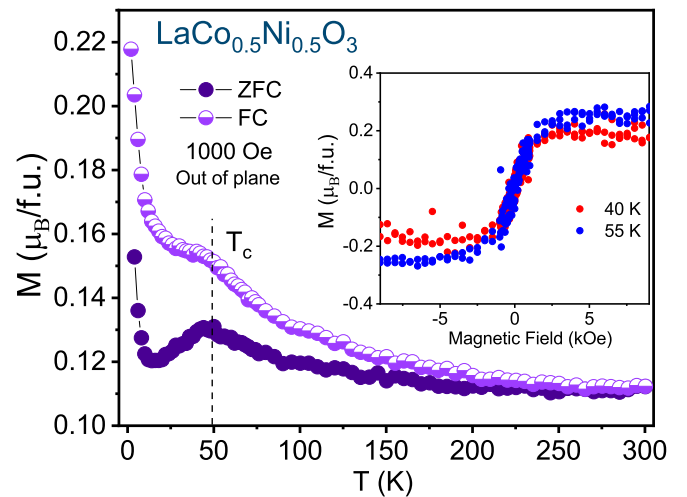

FIG. 4. Magnetization measurements. Zero-field cooled (ZFC) and field cooled (FC) magnetization versus temperature data at 1000 Oe applied field. Inset shows the field-dependent magnetization at 40 and 55 K. The diamagnetic background contribution from STO has been subtracted using the moment values obtained from the $M(H)$ data of bare STO substrate.

ferromagnetism. From Fig. 4 (inset) we can see a small reduction in the saturation magnetization (M_s) from 0.25 μ_B/f.u. at 55 K to around 0.18 μ_B/f.u. at 40 K. The change in the coercive field from 55 to 40 K is indistinguishable due to low signal-to-noise ratio in the measurement of the low-moment sample. To get further insights into spin dynamics across the ferromagnetic transition temperature, we have carried out temperature-dependent x-ray absorption spectroscopy measurements.

E. XAS and XMCD measurements

XAS is a direct method to probe the electronic ground states and give better insights into the spin-state transitions and valence states of cobalt and nickel ions in the LCNO thin film. The unusual temperature dependence of AMR phenomena and their connection to the magnetic behavior of the system can be addressed with temperature-dependent XMCD measurements. Using XAS and XMCD measurements at the Co $L_{2,3}$ and Ni $L_{2,3}$ absorption edges, we have probed the 3d electronic ground states of Co and Ni ions in the system at various temperatures above and below the magnetic transition. The temperature dependence of XAS for the Co L_3 edge is shown in Fig. 5(a). The Co L_3 main peak coincides with the Co^{3+} valence ions, and the shoulder peaks to the left and right coincide with Co^{4+} valency [47,48]. Particularly, a double peak XAS feature at 780 eV and intensified shoulder at 782.5 eV are not seen in the Co L_3 XAS of pure LCO [49]. Hence, we confirm our samples are predominantly with a Co^{3+} state along with a possible Co^{4+} state. A small peak around 777 eV represents Co^{2+} valence which could be due to the presence of oxygen vacancies mostly at the film surface [50]. Figure 6 shows the magnification of the XAS shoulder peaks, clearly showing a right shift of the Co L_3 peak as the temperature is reduced. With reference to the ground states of pure LS Co^{3+} and pure HS Co^{3+} compounds, the
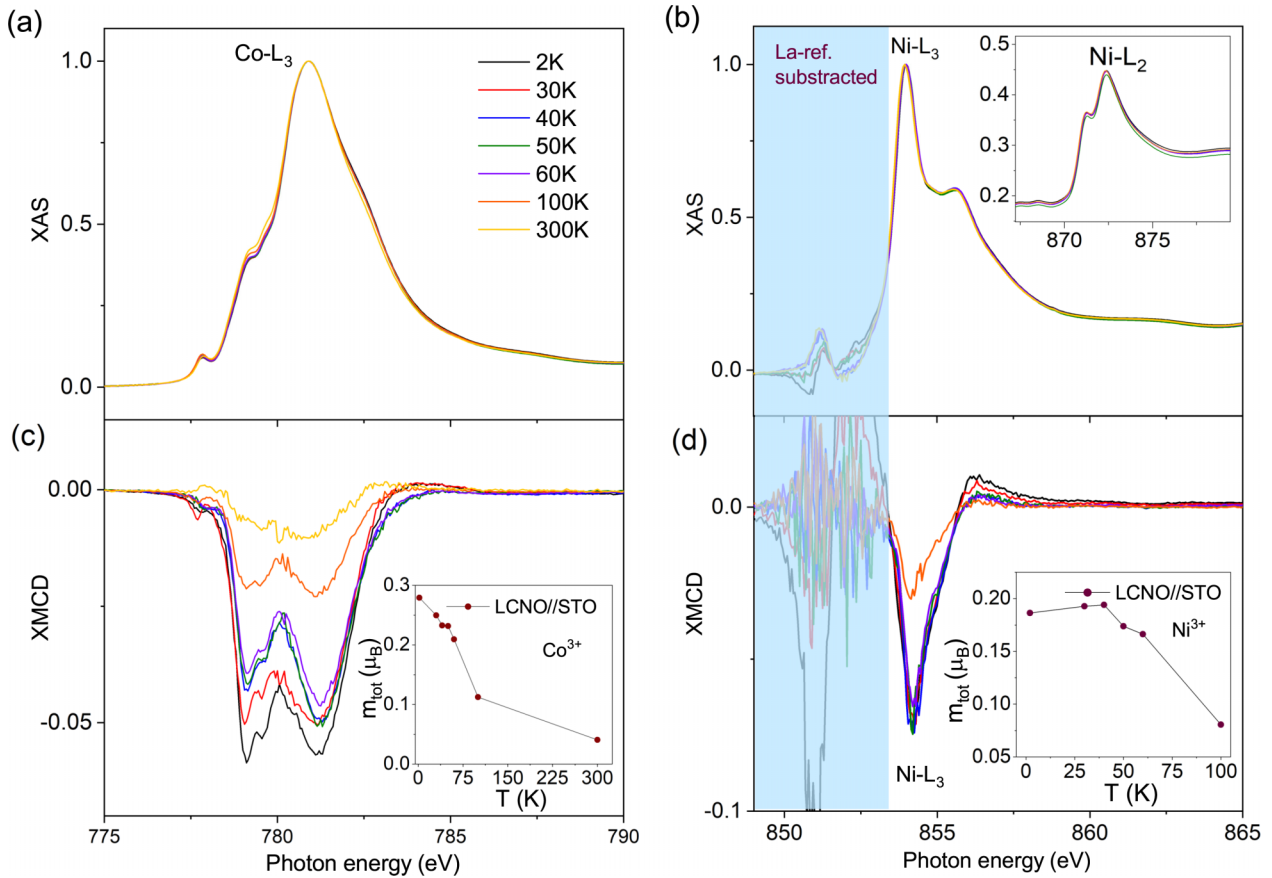
FIG. 5. X-ray absorption spectroscopy. (a) XAS spectra of the Co L_3 edge at different temperatures. (b) XAS spectra of the Ni L_3 edge at different temperatures. The inset shows the XAS spectrum of the Ni L_2 edge. (c) XMCD spectra of the Co L_3 edge at different temperatures. Inset shows the temperature dependence of total magnetic moment derived from the Co L_3-edge XMCD using sum rules. (d) XMCD spectra of the Ni L_3 edge at different temperatures with the inset showing the temperature dependence of total magnetic moment derived from the Ni L_3-edge XMCD using sum rules.
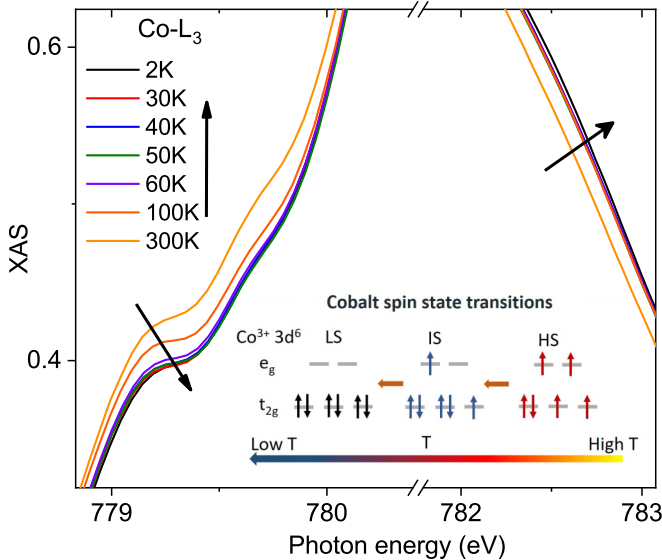

FIG. 6. Spin-state transition. Enlarged view of Co L_3-edge XAS spectra of Fig. 5 showing the peak shift towards the right with a decrease in temperature. The black arrows are a guide to the eyes. Inset shows the schematic of Co spin-state transitions from HS (red) to IS (blue) and then to LS (black) with a decrease in temperature.

corresponding shifts can be inferred as a gradual transition from HS/IS state at 300 K to LS rich state at 2 K [51].

The XMCD data in Fig. 5(c) shows a single peak at 300 K dominated by the HS/IS Co^{3+} ions. As the temperature is reduced, the XMCD peak splits into a doublet with peaks at 779.1 and 781.2, corresponding to possible Co^{3+} and Co^{4+} ions, respectively. The peak splitting is attributed to the charge-transfer mediated increase in the Co valence, i.e., Co^{4+}, which favor ferromagnetic ordering and have transition corresponding to positive AMR at and above 50 K. We note that the peak intensity ratio Co^{4+}/Co^{3+} increases and maximizes at 50 K, coinciding with the ferromagnetic transition temperature obtained from the magnetic measurements using a SQUID magnetometer. Importantly, the Co L_3 XMCD [Fig. 5(c)] is found to be increasing with the decreasing temperature, resulting in a net increment in the Co magnetization. These qualitative changes in the XAS cannot complete the full picture of Co sublattice magnetization because the LCNO system contains multiple Co valent states either in HS or LS configurations. However, the spin (m_s) and orbital (m_l) magnetic moments derived from the XMCD data can provide further insight into the Co magnetization, and the discussion is in the following.

We have determined the m_s and m_l of Co (and Ni) ions by applying the sum rules to the integrated intensities of total

XAS and XMCD spectra [52]. Spin sum rule errors, associated to the core-valence exchange interactions, were properly accounted for the calculations [53]. The most important part of the data is that the obtained $m_{tot}(= m_s + m_l)$ of Co ions from the XMCD data reveals a small but noticeable kink at 50 K as shown in the inset of Fig. 5(c), which is a fingerprint to the possible spin reorientation transitions (due to the Co^{4+}) that are already observed through bulk magnetization measured from the SQUID magnetometer, as shown in Fig. 4. All the magnetic moments reported here are for μ_B/ion. The m_l/m_s of Co is in the range of 0.45–0.53. These are slightly higher values than the pure Co^{4+} (0.4–0.45) and lower than the pure Co^{2+} (0.57) ([48], and references therein). However, the m_l/m_s varies between 0.2 and 0.5 for Co^{3+} ions [51,54]. Our values are in good agreement within the possible range despite that the m_l/m_s of Co^{3+} ions widely differ due to their complex nature of HS-LS switchover. We have furthermore investigated the Ni absorption edges; the data is discussed in the following.

The XAS of the Ni L_3 preedge is overlapping with the La M_4 postedge. We have thus removed the La M peak by subtracting the La M XAS recorded on the LSMO reference sample, leaving out some subtracted traces in the Ni L_3 preedge as shown in Fig. 5(b) for the temperature-dependent Ni $L_{2,3}$ XAS. However, the Ni L_2 edge [Fig. 5(b) inset] has no overlap with the La M edge; therefore, we clearly see the dominant peak at the higher energy side corresponds to Ni^{3+} contribution whereas the Ni^{2+} ion forming the shoulder peak to the left side of the main peak [55]. Unlike the Co L_3 edge, the Ni L_3-edge XAS is found to be independent of temperature and therefore no change in the spin state is expected. The Ni L_3 XMCD [Fig. 5(d)] and further derived m_{tot} value remain almost similar below 60 K [see inset of Fig. 5(b)]. Above 50 K, the Ni moments follow a similar trend to that of Co ions. A total moment including Co and Ni ions is matching well with the magnetization data obtained from the SQUID magnetometer. The effect of strain has a substantial influence on AMR in LCNO as shown in the previous section. To get a better understanding of the strain effects in AMR, temperature-dependent XAS studies of LCNO films grown on STO and LAO substrates were compared. Figure 7 shows the XAS and XMCD spectra of the Co L_3 edge at 2 K of LCNO films grown on tensile strained STO and the compressively strained LAO substrates. The XAS spectrum of LAO-grown film is shifted towards the low-energy side compared to its STO counterpart indicating a reduction in the Co^{4+} valence state, which is a clear indication of the variation of local spin magnetic moments with strain [56]. From the XMCD data in Fig. 7(bottom) we see a clear suppression of the peak at 781.5 eV for LAO-grown film indicating a reduction of Co^{4+} spin states in the system.

X-ray absorption studies of Co and Ni edges confirm the role of cobalt spin-state transitions in tuning the magnetization in the LCNO system while the valence and spin states of Ni ions remain same. Hence the AMR switching observed below $T = 50$ K can be attributed to the change in cobalt spin states, which contribute towards a net change in spin polarization densities by changing the magnetization dynamics across the magnetic transition temperature. The inset of Fig. 6 shows a schematic representation of the temperature-dependent spin-
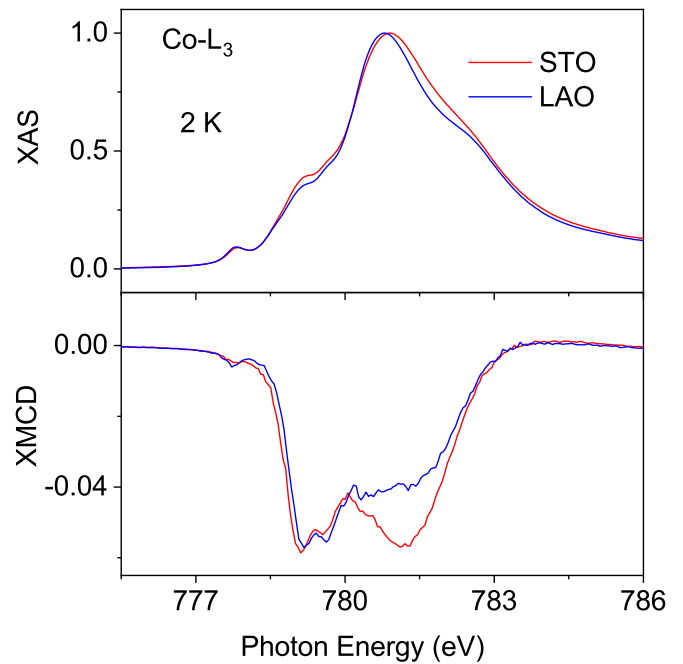

FIG. 7. Strain effects on LCNO: x-ray absorption spectrum. XAS spectrum (top) and XMCD specturm (bottom) of the Co L_3 edge of LCNO grown on STO (red) and LAO (blue) substrates.

state transitions of Co^{3+} ions. The high-temperature region is dominated by the HS state, followed by the IS state at intermediate temperatures and finally, at low temperatures the concentration of the LS state dominate. The existence of Co^{4+} and Ni^{2+} valence states corroborates well with the Ni to Co charge transfer of the type $Ni^{3+} + Co^{3+} \rightarrow Ni^{2+} + Co^{4+}$ in LCNO films and the relative change in the Co^{4+}/Co^{3+} ratio, which is greatly modified by strain, determines the extent of ferromagnetic ordering in the system.

IV. CONCLUSION

In summary, the present study elucidates the tunability of anisotropic magnetoresistance with respect to temperature and strain in LCNO thin films arising from thermally induced Co spin-state transitions. The observed reduction in magnetoconductance and inelastic phase coherence length below the magnetic transition temperature hints towards the onset of a glassy phase, similar to bulk LCNO, due to spin reorientation. In addition, a direct correlation of the magnetic ordering to the magnetoresistance anisotropy can be seen across the ferromagnetic ordering temperature in the form of temperature-dependent sign reversal of AMR. The low-temperature XAS and XMCD measurements performed across AMR switching temperatures shows a Co^{3+} spin-state transition from HS/IS to LS, favoring antiferromagnetic superexchange interaction. Further, we have observed a noticeable reduction in Co^{4+} valence states for compressively strained films, which directly influenced the magnetic ordering in the system affecting the AMR behavior. Compared to the parent LCO and LNO films, LCNO thin films host a complex magnetic phase diagram involving multiple spin and valence states. The intricate magnetic ordering and spin reorientation of LCNO triggered by thermally induced spin-state

transitions can be leveraged to achieve innovative functionalities in heterostructures, especially when combined with materials possessing high spin-orbit coupling.

APPENDIX A: TEMPERATURE DEPENDENCE OF ELECTRICAL RESISTIVITY

$LaNiO_3$ is a paramagnetic metal throughout the temperature range and $LaCoO_3$ is a nonmagnetic insulator in its low-temperature ground state. Therefore, from earlier studies, it is known that $LaCo_{0.5}Ni_{0.5}O_3$ falls near the M-I transition [21,57]. The conduction mechanism in $LaCo_{1-x}Ni_xO_3$ is through O_{2p}-assisted d-d electronic transitions. At high temperatures, the resistivity follows the Arrhenius equation [see Eq. (A3)], while for low enough temperatures, the conduction mechanism is governed by the Mott variable range hopping mechanism [Eq. (A1)].

$$\rho(T) = \rho_o \exp\left(\frac{T_0}{T}\right)^{1/n}, \tag{A1}$$

TABLE I. Resistivity fit parameters for LCNO samples grown on $SrTiO_3$ substrates with various thicknesses.

Film	Mott VRH fit		Arrhenius fit	
thickness[a] (nm)	ρ_o (Ω cm)	T_o (K)	ρ_o' (Ω cm)	E_a (meV)
6	9.23×10^{-9}	8.80×10^{6}	2.02×10^{-3}	44.9
10	2.89×10^{-5}	1.35×10^{5}	1.76×10^{-3}	18.2
25	4.9×10^{-4}	1.08×10^{4}	3.48×10^{-3}	12.0

[a]Films grown on $SrTiO_3$ substrate.

where ρ_0 is the exponential prefactor and T_0 is the Mott characteristic temperature defined as

$$T_o = \frac{18}{k_B N(E_F)\xi^3}, \tag{A2}$$

where k_B is the Boltzmann constant, $N(E_F)$ is the density of states at the Fermi level, and ξ is the localization length. Figure 8(a) shows the temperature dependence of resistivity for the 10-nm LCNO sample. The resistivity plot shows a semiconducting behavior with a steep increase in resistivity towards low temperatures. For temperatures from 4 to 150 K, resistivity data is fitted with Eq. (A1) [see Fig. 8(b)]. In the high-temperature region, i.e., from 150 to 300 K, the resistivity data could be fitted by the phonon-assisted nearest-neighbor hopping interaction process, which is given by the Arrhenius equation as

$$\rho(T) = \rho_o' \exp\left(\frac{E_a}{k_B T}\right). \tag{A3}$$

Further, we have also studied resistivity in films with varying thicknesses of 6, 10, and 25 nm, and the corresponding fit parameters for Eqs. (A1) and (A3) are given in Table I. From Table I, we can see that as the thickness is reduced, activation energy is increased as inferred from the high-temperature Arrhenius fit.
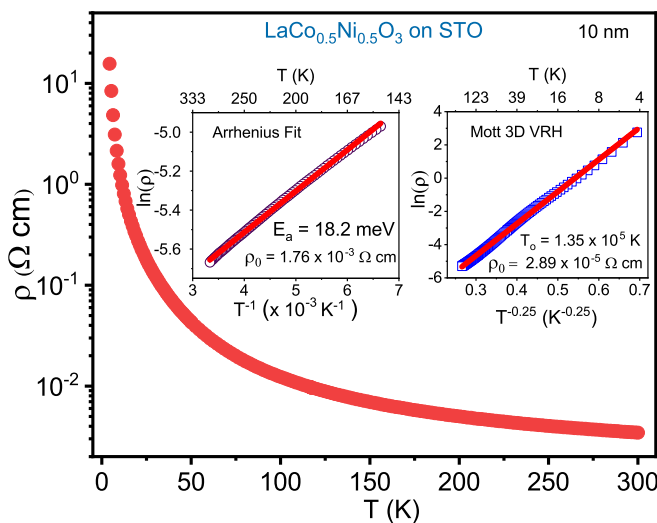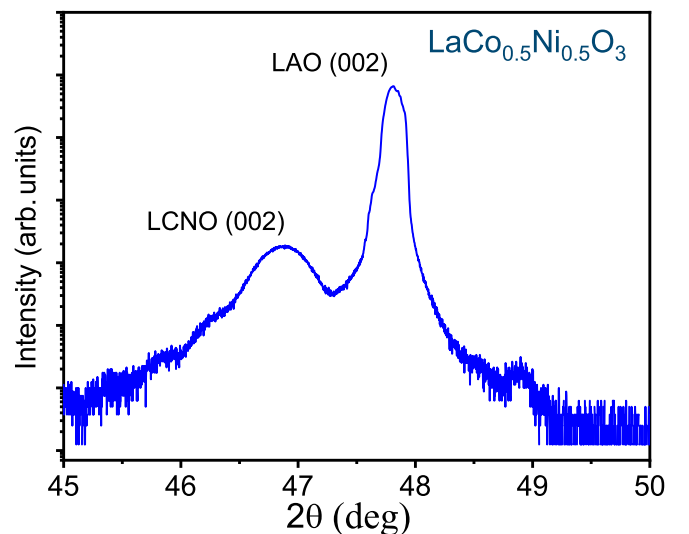

FIG. 8. Electrical transport study. Semilogarithmic-scale plot of resistivity versus temperature data for 10-nm LCNO film. Inset on the right is the 3D Mott variable range hopping (VRH) fit for low-temperature resistivity data from 4 to 150 K and the inset on the left is the Arrhenius fit for the high-temperature data from 150 to 300 K.

FIG. 9. Thin-film XRD data of LCNO film on $LaAlO_3$ substrate with (002) peaks indexed.

APPENDIX B: THIN-FILM XRD OF LCNO
ON LAO SUBSTRATE

Epitaxial films of LCNO were grown on LAO (001) substrates. Figure 9 shows the x-ray diffraction 2θ-ω scan of the LCNO film grown on LAO.

[1] P. W. Anderson and S. F. Edwardst, in *A Career in Theoretical Physics*, 2nd ed., World Scientific Series in 20th Century Physics Vol. 35 (World Scientific, Singapore, 2005), p. 510.

[2] N. P. Armitage, P. Fournier, and R. L. Greene, Rev. Mod. Phys. **82**, 2421 (2010).

[3] A. P. Ramirez, J. Phys.: Condens. Matter **9**, 8171 (1997).

[4] M. Imada, A. Fujimori, and Y. Tokura, Rev. Mod. Phys. **70**, 1039 (1998).

[5] T. R. McGuire and R. I. Potter, IEEE Trans. Magn. **11**, 1018 (1975).

[6] M. Egilmez, K. H. Chow, and J. A. Jung, Mod. Phys. Lett. B **25**, 697 (2011).

[7] T. S. Suraj, G. J. Omar, H. Jani, M. M. Juvaid, S. Hooda, A. Chaudhuri, A. Rusydi, K. Sethupathi, T. Venkatesan, A. Ariando, and M. S. Ramachandra Rao, Phys. Rev. B **102**, 125145 (2020).

[8] M. Vagadia, S. Sardar, T. Tank, S. Das, B. Gunn, P. Pandey, R. Hübner, F. Rodolakis, G. Fabbris, Y. Choi, D. Haskel, A. Frano, and D. S. Rana, Phys. Rev. B **105**, L020402 (2022).

[9] C.-J. Zhao, L. Ding, J.-S. HuangFu, J.-Y. Zhang, and G.-H. Yu, Rare Met. **32**, 213 (2013).

[10] X. Sun, F. Tang, X. Shen, W. Sun, W. Zhao, Y. Han, X. Kan, S. Cong, L. Zhang, Z. Han, B. Qian, X. Jiang, S. Wang, R. Zheng, and Y. Fang, Phys. Rev. B **105**, 195114 (2022).

[11] K. Sreedhar, J. M. Honig, M. Darwin, M. McElfresh, P. M. Shand, J. Xu, B. C. Crooker, and J. Spalek, Phys. Rev. B **46**, 6382 (1992).

[12] M. Karolak, M. Izquierdo, S. L. Molodtsov, and A. I. Lichtenstein, Phys. Rev. Lett. **115**, 046401 (2015).

[13] K. P. Rajeev, G. V. Shivashankar, and A. K. Raychaudhuri, Solid State Commun. **79**, 591 (1991).

[14] X. Q. Xu, J. L. Peng, Z. Y. Li, H. L. Ju, and R. L. Greene, Phys. Rev. B **48**, 1112 (1993).

[15] R. R. Heikes, R. C. Miller, and R. Mazelsky, Physica **30**, 1600 (1964).

[16] M. A. Korotin, S. Y. Ezhov, I. V. Solovyev, V. I. Anisimov, D. I. Khomskii, and G. A. Sawatzky, Phys. Rev. B **54**, 5309 (1996).

[17] P. M. Raccah and J. B. Goodenough, Phys. Rev. **155**, 932 (1967).

[18] Y. Tokura, Y. Okimoto, S. Yamaguchi, H. Taniguchi, T. Kimura, and H. Takagi, Phys. Rev. B **58**, R1699 (1998).

[19] C. S. Naiman, R. Gilmore, B. Dibartolo, A. Linz, and R. Santoro, J. Appl. Phys. **36**, 1044 (1965).

[20] Y. Ren, J.-Q. Yan, J.-S. Zhou, J. B. Goodenough, J. D. Jorgensen, S. Short, H. Kim, T. Proffen, S. Chang, and R. J. McQueeney, Phys. Rev. B **84**, 214409 (2011).

[21] D. Hammer, J. Wu, and C. Leighton, Phys. Rev. B **69**, 134407 (2004).

[22] V. Narasimhan, H. V. Keer, and D. K. Chakrabarty, Phys. Status Solidi A **89**, 65 (1985).

[23] M. Viswanathan and P. S. Anil Kumar, Phys. Rev. B **80**, 012410(R) (2009).

[24] J. Pérez, J. García, J. Blasco, and J. Stankiewicz, Phys. Rev. Lett. **80**, 2401 (1998).

[25] G. H. Jonker and J. H. Van Santen, Physica **19**, 120 (1953).

[26] T. Motohashi, V. Caignaert, V. Pralong, M. Hervieu, A. Maignan, and B. Raveau, Phys. Rev. B **71**, 214424 (2005).

[27] T. Asaba, Z. Xiang, T. H. Kim, M. S. Rzchowski, C. B. Eom, and L. Li, Phys. Rev. B **98**, 121105(R) (2018).

[28] A. J. Millis, T. Darling, and A. Migliori, J. Appl. Phys. **83**, 1588 (1998).

[29] K. Nishio and T. Tsuchiya, in *Handbook of Sol-Gel Science and Technology* (Springer International Publishing, New York, 2018), pp. 133–154.

[30] A. Barla, J. Nicolás, D. Cocco, S. M. Valvidares, J. Herrero-Martín, P. Gargiani, J. Moldes, C. Ruget, E. Pellegrin, and S. Ferrer, J. Synchrotron Radiat. **23**, 1507 (2016).

[31] M. Björck and G. Andersson, J. Appl. Cryst. **40**, 1174 (2007).

[32] S. Wang and P. E. Lindelof, J. Low Temp. Phys. **71**, 403 (1988).

[33] S. Hikami, A. I. Larkin, and Y. Nagaoka, Prog. Theor. Phys. **63**, 707 (1980).

[34] W. Wei, G. Bergmann, and R. P. Peters, Phys. Rev. B **38**, 11751 (1988).

[35] R. P. Peters, G. Bergmann, and R. M. Mueller, Phys. Rev. Lett. **60**, 1093 (1988).

[36] F. Schopfer, C. Bäuerle, W. Rabaud, and L. Saminadayar, Phys. Rev. Lett. **90**, 056801 (2003).

[37] A. W. Rushforth, K. Výborný, C. S. King, K. W. Edmonds, R. P. Campion, C. T. Foxon, J. Wunderlich, A. C. Irvine, P. Vašek, V. Novák, K. Olejník, J. Sinova, T. Jungwirth, and B. L. Gallagher, Phys. Rev. Lett. **99**, 147207 (2007).

[38] M. V. Kartsovnik, V. N. Laukhin, S. I. Pesotskii, I. F. Schegolev, and V. M. Yakovenko, J. Phys. I **2**, 89 (1992).

[39] D. Wu, P. Wei, E. Johnston-Halperin, D. D. Awschalom, and J. Shi, Phys. Rev. B **77**, 125320 (2008).

[40] P. Li, C. Jin, E. Y. Jiang, and H. L. Bai, J. Appl. Phys. **108**, 093921 (2010).

[41] Y. Z. Chen, J. R. Sun, T. Y. Zhao, J. Wang, Z. H. Wang, B. G. Shen, and N. Pryds, Appl. Phys. Lett. **95**, 132506 (2009).

[42] A. P. Malozemoff, Phys. Rev. B **32**, 6080 (1985).

[43] I. A. Campbell, A. Fert, and O. Jaoul, J. Phys. C: Solid State Phys. **3**, S95 (1970).

[44] S. Kokado, M. Tsunoda, K. Harigaya, and A. Sakuma, J. Phys. Soc. Jpn. **81**, 024705 (2012).

[45] T. Kyômen, R. Yamazaki, and M. Itoh, Phys. Rev. B **68**, 104416 (2003).

[46] T. Kyômen, Y. Asaka, and M. Itoh, Phys. Rev. B **67**, 144424 (2003).

[47] H.-J. Lin, Y. Y. Chin, Z. Hu, G. J. Shu, F. C. Chou, H. Ohta, K. Yoshimura, S. Hébert, A. Maignan, A. Tanaka, L. H. Tjeng, and C. T. Chen, Phys. Rev. B **81**, 115138 (2010).

[48] F. Guillou, K. Kummer, Y. Bréard, L. Hervé, and V. Hardy, Phys. Rev. B **95**, 174445 (2017).

[49] S.-C. Liao, S. C. Haw, C. Y. Kuo, H. Guo, H. B. Vasili, S. M. Valvidares, A. C. Komarek, H. Ishii, S. A. Chen, H. J. Lin, A. Tanaka, T. S. Chan, L. H. Tjeng, C. T. Chen, Z. Hu, and J. M. Chen, Phys. Rev. B **99**, 075110 (2019).

[50] J.-M. Chen, Y.-Y. Chin, M. Valldor, Z. Hu, J.-M. Lee, S.-C. Haw, N. Hiraoka, H. Ishii, C.-W. Pao, K.-D. Tsuei, J.-F. Lee, H.-J. Lin, L.-Y. Jang, A. Tanaka, C.-T. Chen, and L. H. Tjeng, J. Am. Chem. Soc. **136**, 1514 (2014).

[51] M. W. Haverkort, Z. Hu, J. C. Cezar, T. Burnus, H. Hartmann, M. Reuther, C. Zobel, T. Lorenz, A. Tanaka, N. B. Brookes, H. H. Hsieh, H.-J. Lin, C. T. Chen, and L. H. Tjeng, Phys. Rev. Lett. **97**, 176405 (2006).

[52] Q. Shen, H. Luo, and J. K. Furdyna, Phys. Rev. Lett. **75**, 2590 (1995).

[53] C. Piamonteze, P. Miedema, and F. M. F. de Groot, Phys. Rev. B **80**, 184410 (2009).

[54] M. Merz, P. Nagel, C. Pinta, A. Samartsev, H. v. Löhneysen, M. Wissinger, S. Uebe, A. Assmann, D. Fuchs, and S. Schuppler, Phys. Rev. B **82**, 174416 (2010).

[55] C. Piamonteze, M. Gibert, J. Heidler, J. Dreiser, S. Rusponi, H. Brune, J.-M. Triscone, F. Nolting, and U. Staub, Phys. Rev. B **92**, 014426 (2015).

[56] J. Freeland, J. Ma, and J. Shi, Appl. Phys. Lett. **93**, 212501 (2008).

[57] A. K. Raychaudhuri, Adv. Phys. **44**, 21 (1995).